Journal of Engineering Science and Technology Review 17 (5) (2024) 1-7

Research Article

JOURNAL OF
Engineering Science and Technology Review

www.jestr.org

Experimental and Theoretical Investigation of GS-441524 using Density Functional Theory, FTIR, Raman and UV-VIS Spectroscopy

Nektaria Georgopoulou[1], Ita Necitailaite[2], Constantinos D. Zeinalipour-Yazdi[2,3], Dimitrios Palles[4], George Mousdis[4], Christos Garoufalis[5] and Sarantos Marinakis[1,*]

[1]*Department of Chemistry, University of Patras, University Campus, GR-26504 Rion, Achaia, Greece*
[2]*Department of Chemistry, University of East London, Stratford Campus, Water Lane, London E15 4LZ, UK*
[3]*Faculty of omputing, Mathematics, Engineering and Natural Sciences, Northeastern University London, London, E1W 1LP, UK*
[4]*Theoretical and Physical Chemistry Institute, National Hellenic Research Foundation, 48 Vassileos Constantinou Ave., 11635 Athens, Greece*
[5]*Department of Materials Science, University of Patras, University Campus, GR-26504 Rion, Achaia, Greece*

Received 1 September 2024; Accepted 13 October 2024

Abstract

GS-441524, a 1′ substituted C glycoside and an adenosine analogue, exhibits broad antiviral activity against RNA viruses. Previous research has primarily concentrated on its antiviral properties for humans and animals. Vibrational and electronic spectroscopy can enhance our understanding of its structure and function and serve as valuable tools in detection techniques and kinetic studies. In this paper, we employed IR and Raman spectroscopy to study its solid form, and UV-VIS spectroscopy to examine its aqueous solution. Density Functional Theory (DFT) calculations were utilized to analyze the spectra. Specifically, we evaluated the DFT functionals B3LYP, BP86, and CAM-B3LYP in conjunction with the basis sets 6-31G(d,p), 6-311G(d,p), and 6-311++G(d,p). The largest basis set, 6-311++G(d,p), performed significantly better than the smaller ones in reproducing the experimental results. The BP86 functional most accurately reproduced the vibrational spectra, while B3LYP best matched the electronic spectra. By increasing the basis set size, disregarding the Tamm-Dancoff approximation (TDA), and accounting for solvent effects using the polarizable continuum model, the wavelength, λmax, of the largest peak in the UV-VIS calculations, shifted (increased) by 2, 7.5, and 18 nm towards the experimental value, respectively.

Keywords: GS-441524; IR; Raman; UV-VIS; DFT; Feline Infectious Peritonitis

1. Introduction

Nucleoside analogues, in general, show antiviral activity against a variety of viruses including those of HIV, Hepatitis B and C among others [1]. The way they work as antiviral agents is by mimicking the nucleosides normally found in viruses and thus affecting the DNA or RNA synthesis. When in drugs, they are generally considered safe and well tolerated since they only affect the virus polymerases but not the human ones. Specifically, they either block polymerase's activity or lead to the termination of nucleic acid synthesis [2].

GS-441524 is a nucleoside analogue of adenosine which shows great antiviral properties. The skeletal structure of GS-441524 is shown in Fig. 1. It is structurally considered a C nucleoside, as it consists of one 1′ substituted ribose which bonds to a heterocyclic base by a C glycosidic bond, in contrast to the N glycosidic bond found in most nucleosides. 1′ substituted C nucleosides are shown to be very effective against various RNA viruses [3].

GS-441524 has been proven to be an effective treatment against a variety of RNA and DNA viruses such as the African Swine Fever Virus (ASFV) and SARS-CoV among others [4], [5]. Its most common target is feline coronavirus (FCoV), an RNA virus, which is responsible for feline infectious peritonitis, a lethal disease in cats [6], [7], [8]. The infection is highly contagious, especially amongst cats in catteries and shelters that have common food sources and litter facilities [9], [10].

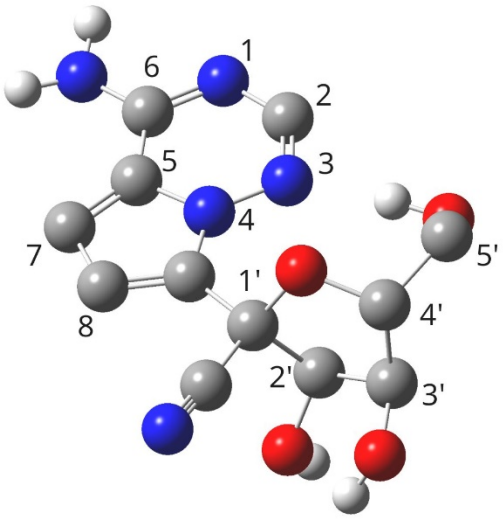

Fig. 1. Skeletal formula of GS-441524. The atoms in the heterocyclic base are numbered 1-9, while the atoms in the substituted ribose are numbered using primed numbers 1′-5′.

GS-441524 was found to be non-toxic in cats at dosages up to 100 μM and effectively inhibited FIP virus replication at dosages as low as 1 μM [3]. However, it has remained a non-approved treatment in many countries, leading many cat

*E-mail address: s.marinakis@upatras.gr
ISSN: 1791-2377
doi:10.25103/jestr.175.01

owners to obtain it from the black market and use it as a last resort, as there have been cases of cats recovering due to GS-441524 reducing viral replication [11]. More recently, it has become legally available to veterinarians in the UK and Australia [12], [13]. GS-441524 aids in treating the infection by blocking the RNA-dependent RNA polymerase (RdRp) of the virus, thereby causing termination of the RNA synthesis and minimizing the polyprotein destruction in cells caused by the virus [3].

GS-441524 was developed by Gilead Sciences, which is an American biopharmaceutical company that specializes in researching and developing antiviral drugs [14]. However, Gilead Sciences has not pursued the development of GS-441524, halting its progress [15]. In 2019, the very first pill of GS-441524 came out by the Chinese company Mutian Life Sciences Co., Ltd named Mutian® Xraphconn targeting FIP, which became available in Asia [16].

Due to the COVID-19 pandemic, GS-441524 has also been the subject of research to determine its potential as a treatment for the disease. Studies have indicated that it effectively reduced viral load and have suggested that when phosphorylated, GS-441524 can mimic the normal substrates of SARS-CoV-2's RdRp, such as ATP. This resemblance leads to the delayed termination of RNA synthesis and ultimately results in the virus's demise [3]. Typically, the antiviral activity of GS-441524 and other nucleoside analogues becomes activated following phosphorylation by deoxyribonucleoside kinases, nucleoside monophosphate kinases (NMPKs), and nucleoside diphosphate kinases (NDPKs) [17].

While numerous research papers have delved into the medicinal and veterinary application of GS-441524, there remains a dearth of published work focusing on its spectroscopy. Consequently, this study aims to bridge the gap by presenting a comprehensive examination of its vibrational (infrared and Raman) and electronic (UV-VIS) spectroscopy through a combined experimental and theoretical approach. Our in-experimental findings are detailed and juxtaposed with density functional theory (DFT) calculations for comparison.

2. Methods

2.1. Experimental Methods

2.1.1. Infrared Attenuated Total Reflectance (ATR)

Solid GS-441524 was procured from Activate Scientific and utilized without further modification for all the measurements. The attenuated total reflection (ATR) spectra were recorded within the range of 525-5000 cm^{-1} using a 45° single bounce diamond crystal ATR accessory (Pike Technologies, MIRacle) attached to a Fourier-Transform mid-infrared spectrometer (Equinox 55 by Bruker Optics) set to operate at a resolution of 4 cm^{-1}. In ATR, akin to other infrared techniques, the spatial (xy) resolution, representing the ability to differentiate between different phases, is ca. 5-10 μm.

The average probing depth, dependent on wavelength, is typically a few μm due to the evanescent field of the infrared beam's total reflection from the diamond crystal, which is in direct contact with the sample. The sample is held in contact with the diamond using a mechanical hand-operated press with adjustable fixed pressure. Our ATR accessory features a circular disk sampling area of 1.8 mm diameter, rendering ATR a surface-sensitive method for bulk characterization spectroscopy, particularly advantageous for powder analysis. Unlike conventional infrared transmittance measurements, this method necessitates no sample preparation and avoids issues such as absorption saturation or hydrolysis/ion-exchange effects, which may arise from mixing with KBr or a similar matrix. The data within the frequency range of 1950-2700 cm^{-1} may contain artifacts from the diamond accessory and carbon dioxide from the atmosphere, and hence, are not displayed.

2.1.2. Micro-Raman spectroscopy

The Raman spectra were collected across the range of 100-4000 cm^{-1} utilizing a dispersive confocal Raman spectrometer (InVia Reflex by Renishaw) equipped with a microscope and a Peltier-cooled CCD camera, operating at a resolution of 1 cm^{-1}. A solid-state laser emitting at the 785 nm line was employed for excitation, maintaining the power on the sample below ca. 4.2 mW. An objective lens with a ×50 long working distance (N.A. = 0.50) was utilized. The nominal spatial resolution is of the order of 1 μm (for a circular laser beam), while the sampling area of our laser beam is rectangular measuring approximately 20×4 μm. The unpolarized spectra presented herein were captured from a single micro-crystallite of the sample.

2.1.3. UV-VIS spectroscopy

The UV-VIS absorption spectra were recorded at room temperature using a UV-VIS-NIR spectrophotometer (Lambda 19 by Perkin-Elmer) with a resolution of 2 nm. Approximately 3 mL of three different concentrations of GS-441524 solutions (0.0129, 0.0257 and 0.0514 mg/mL) were placed in a 1-cm-long quartz cuvette. The measurements were conducted over the range of 200–1200 nm, as water absorbs strongly above 1400 nm, which would result in very noisy spectra. The scan speed was set to 480 nm/min, and a cuvette containing distilled water was used as a reference.

2.2. Computational Methods

The molecular formula of GS-441524 is $C_{12}H_{13}N_5O_4$, comprising 34 atoms and 152 electrons. Theoretical DFT calculations were performed to determine the optimized three-dimensional geometry and the spectroscopic properties of GS-441524. The initial geometry was based on the atomic coordinates provided in the crystallographic file by Wei et al. [18]. The structural formula of GS-441524 and the atomic labelling scheme are depicted in Fig. 2. The stereochemistry of the four chiral centers was determined to be 2R, 3R, 4S, and 5R, resulting in the molecular configuration: (2R,3R,4S,5R)-2-(4-aminopyrrolo[2,1-f] [1,2,4] triazin-7-yl)-3,4-dihydroxy-5-(hydroxymethyl)oxolane-2-carbonitrile.

All calculations were conducted using the Gaussian 16W program, version 1.1 [19], with visualizations carried out using the GaussView, version 6.1 [20]. The calculations employed the B3LYP [21], BP86 [22], CAM-B3LYP [23] functionals in conjunction with the 6-31G(d,p), 6-311G(d,p), and 6-311++G(d,p) basis sets. The X, Y, and Z coordinates of the optimized geometries are reported in the supporting information section (Tables S1-S3) for the B3LYP, BP86, and CAM-B3LYP functionals, respectively, using the 6-311++G(d,p) basis set. The solvent effects were calculated using the default polarizable continuum model (PCM) [24]. Solvent effects were considered for all the calculations of the UV-VIS spectra, while the calculations for the vibrational spectra were performed in the gas phase. The Fukui functions were extracted using the Gabedit 2.5.1 software [25].

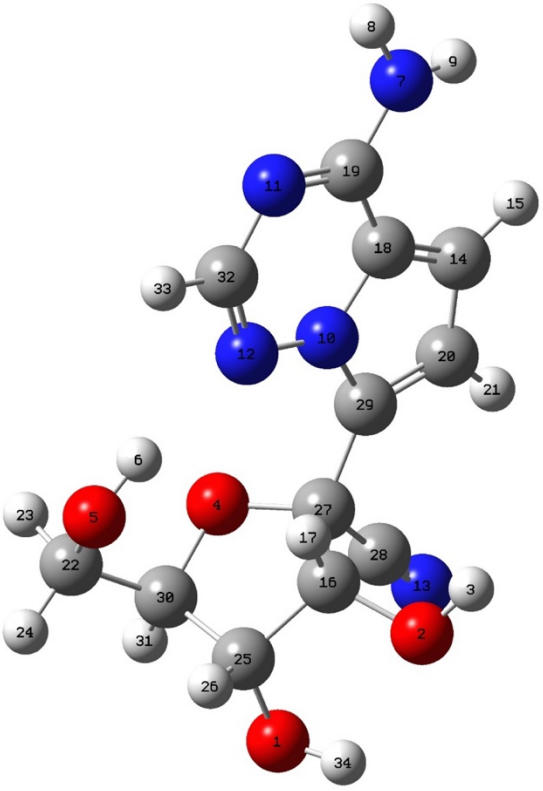

Fig. 2. Structure of GS-441524. The atomic labelling scheme is as used in the calculations in this work (Color online; H, C, N, O atoms are depicted as white, grey, blue, and red spheres, respectively).

3. Results and Discussion

The experimental infrared (IR) spectrum of solid GS-441524 is shown in Fig. 3, and the experimental Raman spectrum is presented in Fig. 4. A comparison between the experimental peaks and the theoretical predictions from all functionals using the largest basis set, 6-311++G(d,p), is also included. The BP86 functional provided the best reproduction of the IR and Raman experimental data, showing the lowest overall frequency deviations between experimental and theoretical values compared to the B3LYP and CAM-B3LYP functionals.

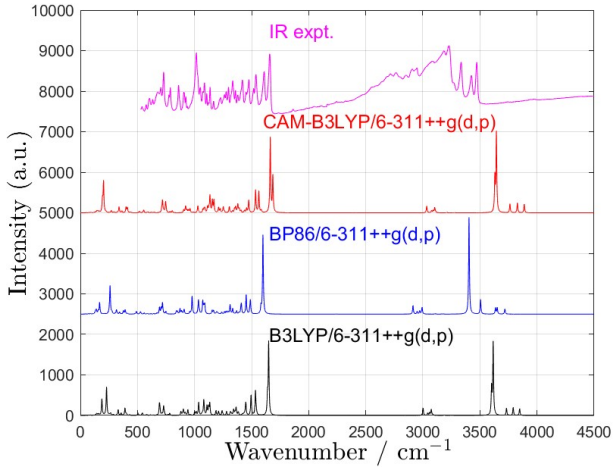

Fig. 3. Comparison between the experimental infrared spectrum of solid GS-441524 and theoretical calculations using the B3LYP/6-311++G(d,p), BP86/6-311++G(d,p), and CAM-B3LYP/6-311++G(d,p) levels of theory. The theoretical spectra have been shifted along the intensity axis by 2500 (a.u.) and the experimental spectrum was scaled by (2000/0.45)-250 to facilitate comparison.

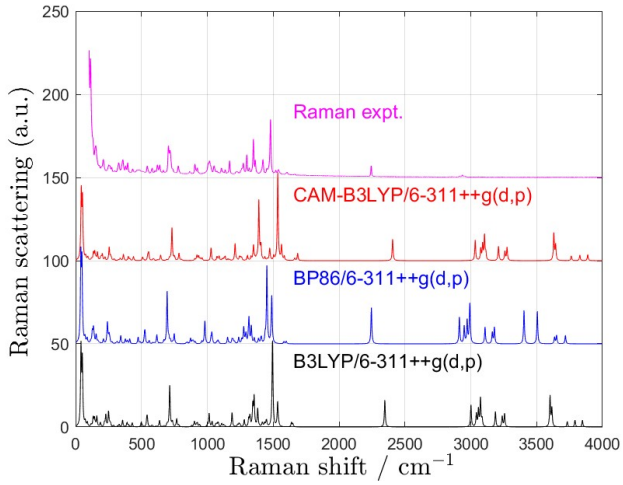

Fig. 4. Comparison between the experimental Raman spectrum of solid GS-441524 and theoretical calculations using the B3LYP/6-311++G(d,p), BP86/6-311++G(d,p), and CAM-B3LYP/6-311++G(d,p) levels of theory. The theoretical spectra have been shifted along the intensity axis by 50 (a.u.), and the experimental spectrum was divided by 2000 and displaced by 150 (a.u.) to facilitate comparison.

The vibrational assignment of 37 infrared and 33 Raman experimental peaks, along with a comparison to BP86 predictions, is detailed in Table S4. Peak assignments were primarily made using Socrates [26], in addition to references [27], [28], and GaussView 6.1 for the animations of the normal modes of vibrations. In the 0-1000 cm^{-1} region, the experimental frequencies are slightly higher than the theoretical ones, with BP86 being closest to the experimental values. In the 1000-2000 cm^{-1} region, there is a good agreement between the experimental values and those predicted by each of the three DFT methods, with B3LYP values being closest to the experimental data. In the 2000-4000 cm^{-1} region, the experimental frequencies are lower than the theoretical predictions, but the BP86 method shows the best overall comparison with the experimental data in this region and across the entire spectrum.

In Figure 4, a comparison between the experimental Raman spectrum of solid GS-441524 and the DFT calculations is displayed. The agreement between theoretical and experimental values is highly satisfactory. The comparison between theory and experiment in the assignment of the vibrational modes in Table 1 utilizes predictions from the BP86 functional, as this method demonstrates overall better agreement with the experiments. Despite the DFT calculations modeling the isolated molecule in the gas phase, the agreement between the theory and experiment is notably strong.

The experimental UV-VIS spectra of aqueous solutions of GS-441524 at concentrations of 0.0129, 0.0257, and 0.0514 mg / mL are shown in Fig. 5. The spectrum obtained from the 0.0129 mg/ml solution will be used for comparison with theoretical predictions, as its absorbance value is closest to the acceptable range (near 1). The global maximum appears around 245 nm, with two additional, albeit lower and broader, local maxima at approximately 213 and 276 nm. Our experimental values for the molar extinction coefficient, ε (M^{-1} cm^{-1}) are 38378 at 245 nm and 35461 at 240 nm. These values are somewhat higher than those reported by Mulligan and Browning [29], who found 25336 at 245 nm and 31710 at 240 nm. This discrepancy may arise from various factors, such as potential impurities in the samples used in this work or in [29], which could absorb around 240 nm similar to GS-

441524, the lower resolution (5 nm) in [29] compared to this work (2 nm), solubility issues, and measuring absorbances at values significantly greater than 1, indicating that the solutions were too concentrated.

Table 1. Assignment of the most characteristic experimental (in cm^{-1}) infrared and Raman bands. More details regarding the assignment, intensities, and widths of the peaks are provided in the supporting information section (Table S4).

Infrared	Raman	Peak assignment
3471	-	O-H stretch
3425	-	O-H stretch
3334	-	N-H stretch (asym.)
3228	-	N-H stretch (sym.)
3084	3056	C-H stretch
2243	2245	-C≡N stretch
1658,1610	1664, 1605	N-H deformation (triazine, aromatic ring), C=N stretching
1539 with a shoulder at 1518	1541, 1519	stretching of aromatic ring
1016	1016	In-plane deformation of aromatic rings, C-O stretching alcohols, tetrahydrofurans
729	717	stretching of aromatic rings

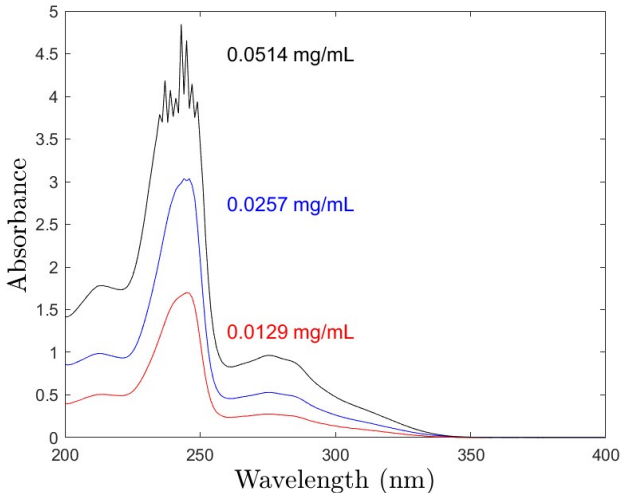

Fig. 5. UV-VIS spectra of aqueous solutions of GS-441524 at various concentrations (shown in the figure).

A comparison of molar extinction coefficients, ε (M^{-1} cm^{-1}), between B3LYP, BP86, and CAM-B3LYP using the 6-311++G(d,p) basis set is presented in Fig. 6 along with the experimental absorbance values. The B3LYP functional reproduces the position of the highest peak, λ_{max}, and the overall shape of the experimental curve better than the other two functionals. The effect of the basis set size on λ_{max} is small. For example, in B3LYP calculations without accounting for the solvent, the λ_{max} values (in nm) were 213.61, 214,9, and 216.96 for 6-31G(d,p), 6-311G(d,p), and 6-311++G(d,p), respectively. When accounting for the solvent using the polarizable continuum model (PCM) [24], λ_{max} shifted to 234.6. By disregarding the Tamm-Dancoff approximation (TDA) [30], the value became 242.03, in excellent agreement with the experimental value. The TDA (Tamm-Dancoff approximation) simplifies the TD-DFT equations by neglecting certain off-diagonal elements that involve interactions between electronic excitation and de-excitation processes. Therefore, the full TD-DFT approach may lead to improved accuracy in calculating of transition frequencies and oscillator strengths, especially in systems with strong electron correlations or complex excited-state dynamics.

The shapes of the HOMO-1 (orbital with cardinal number 75a), HOMO (76a), LUMO (77a), and LUMO+1 (78a) orbitals from the B3LYP/6-311++G(d,p) calculations in aqueous solution are shown in Fig. 7. The electron transition between the HOMO and LUMO orbitals corresponds to 0.17677 eV. The calculated UV-VIS stick spectrum has a maximum with an oscillator strength (f) of 0.6890, at 242.03 nm, consisting of the following transitions (with coefficients in parentheses): 73a→77a (0.11567), 75a→77a (0.44624), 76a→78a (0.47624), and 76a→80a (-0.14116). Additionally, the second highest peak is at 218.72 nm with f = 0.0784, consisting of: 71a→77a (0.13965), 72a→77a (0.12535), 75a→77a (0.10034), 76a→79a (-0.11200), 76a→80a (0.59832), and 76a→81a (-0.24787). The third highest peak is at 270.13 nm with f = 0.0481, consisting of: 75a→77a (0.46060), 76a→77a (0.29727), and 76a→78a (-0.42871). These three highest theoretical peaks are within about 5 nm of the experimental values. As indicated in the orbital shapes in Fig. 7, π←π* transitions play a significant role in the peaks.

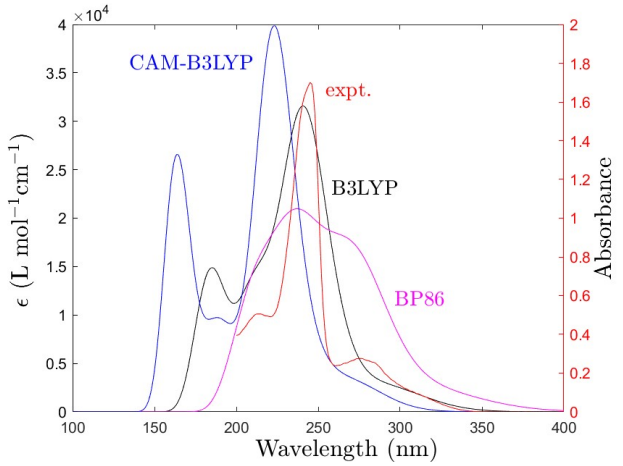

Fig. 6. Comparison between the experimental UV-VIS absorbance (red color) of a 0.0129 mg/mL GS-441524 solution in water and the theoretical predictions of ε (L mol^{-1} cm^{-1}) from B3LYP (black), BP86 (magenta), and CAM-B3LYP (blue) calculations using the 6-311++G(d,p) basis set.

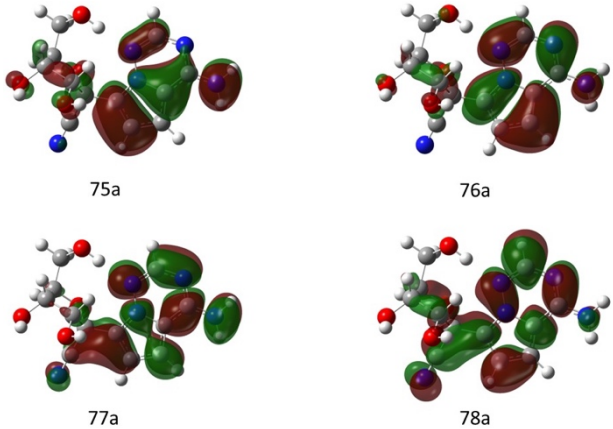

Fig. 7. The frontier molecular orbitals of GS-441524 from B3LYP/6-311++G(d,p) calculations in aqueous solution: HOMO-1 (75a) -0.25645 eV, HOMO (76a) -0.23840 eV, LUMO (77a) -0.06163 eV, LUMO+1 (78a) -0.03591 eV.

Fukui functions are crucial tools in computational chemistry for understanding the reactivity of molecules [31]. The function, $f(r)$, describes the change in the electron density at a specific point r, when the number of electrons in the system changes slightly. We have calculated the f_k^+(for nucleophilic attack), f_k^- (for electrophilic attack), f_k^0(the

average of f_k^+ and f_k^-), and the difference $f_k^+ - f_k^-$. All the values are shown in Table 2. We note that the atom O4 has the largest value for nucleophilic attack, while C28 and C29 have the largest values for electrophilic and radical attack.

Table 2. Local reactivity descriptors of GS-441524 calculated at the B3LYP/6-311++G(d,p) level of theory in water solvent.

Atom	Fukui functions			
	Nucleophilic attack (f_k^+)	Electrophilic attack (f_k^+)	Radical attack (f_k^0)	$\Delta f = f_k^+ - f_k^-$
O1	-0.012147	0.110109	0.048981	0.122256
O2	0.296754	0.076793	0.186774	-0.219961
H3	0.009220	-0.000025	0.004598	-0.009245
O4	0.431303	0.037669	0.234486	-0.393634
O5	0.096580	0.188304	0.142442	0.091724
H6	0.219240	0.004512	0.111876	-0.214728
N7	-0.009692	0.008563	-0.000564	0.018255
H8	-0.000163	0.011269	0.005553	0.011432
H9	0.000323	0.002325	0.001324	0.002002
N10	-0.005287	0.000569	-0.002359	0.005857
N11	0.001339	0.002474	0.001906	0.001135
N12	0.020563	-0.004812	0.007875	-0.025374
N13	0.034618	0.083711	0.059164	0.049093
C14	0.003978	0.008481	0.006229	0.004503
H15	0.002880	-0.000174	0.001353	-0.003053
C16	0.134032	0.181630	0.157831	0.047598
H17	0.003043	0.000174	0.001608	-0.002869
C18	0.125242	0.274809	0.200026	0.149567
C19	0.205179	0.130960	0.168070	-0.074219
C20	0.141517	0.070630	0.106073	-0.070886
H21	0.000888	0.046052	0.023470	0.045164
C22	0.003637	0.062499	0.033068	0.058862
H23	0.071932	0.014035	0.042984	-0.057896
H24	0.103535	0.082909	0.093222	-0.020626
C25	-0.000098	0.054102	0.027002	0.054201
H26	0.389546	0.197410	0.293478	-0.192136
C27	0.030229	0.133472	0.081851	0.103243
C28	0.073016	1.266965	0.669991	1.193949
C29	0.129570	1.204244	0.666907	1.074674
C30	0.026497	0.053608	0.040052	0.027111
H31	0.000498	0.000807	0.000652	0.000309
C32	0.003259	0.003429	0.003344	0.000170
H33	0.000282	0.000915	0.000598	0.000633
H34	-0.012489	-0.000687	-0.006588	0.011802

Partial charge analysis was also performed for the GS-441524 in water at B3LYP/6-311++G(d,p) level of theory. Mulliken atomic charges of the neutral, cationic, and anionic forms of GS-4415424 are shown in Table 3. The partial charges for various schemes such as Mulliken, CHelp [32], CHelpG [33], HLYGAt [34] but using Gaussian's standard atomic densities instead of those of HLY [34], and according to Merz-Singh-Kollman, MK [35], [36] are shown in Table S5 and a surface plot of the electrostatic potential is shown in Fig. S1.

Table 3. Mulliken atomic charges of the neutral, cationic, and anionic forms of GS-441524.

Atom	Neutral	Cation	Anion
O1	-0.226534	-0.216163	-0.232386
O2	-0.274071	-0.251912	-0.268076
H3	0.312760	0.315079	0.305662
O4	-0.058908	-0.037990	-0.064570
O5	-0.381642	-0.331616	-0.418867
H6	0.433436	0.375656	0.474521
N7	-0.392493	-0.308062	-0.405238
H8	0.354506	0.382324	0.278614
H9	0.318726	0.342831	0.257166
N10	0.584084	0.623510	0.563800
N11	-0.239521	-0.089290	-0.329558
N12	-0.401223	-0.198293	-0.604505
N13	-0.282268	-0.247954	-0.311253
C14	-0.284529	-0.088383	-0.436629
H15	0.214370	0.283070	0.177131
C16	-0.735631	-0.626226	-0.757769
H17	0.275624	0.283275	0.279946
C18	0.399941	0.325411	0.486529
C19	-0.211908	-0.295480	-0.456142
C20	-0.129412	0.007003	-0.155947
H21	0.202351	0.249451	0.173344
C22	-0.703041	-0.726853	-0.684746
H23	0.186895	0.196278	0.174404
H24	0.185752	0.200458	0.171574
C25	-0.565745	-0.627099	-0.507637
H26	0.269021	0.281236	0.254476
C27	0.829064	0.740908	0.705371
C28	-0.802811	-0.834461	-0.748229
C29	-0.310310	-0.210027	-0.297750
C30	0.601499	0.591398	0.618892
H31	0.287308	0.305364	0.270316
C32	0.034425	0.023146	0.026850
H33	0.234083	0.283017	0.185880
H34	0.276202	0.280392	0.274828

4. Conclusions

In summary, the GS-441524 molecule was studied using DFT calculations alongside IR, Raman, and UV-VIS spectroscopy. The theoretical calculations provided the optimized three-dimensional geometry of the molecule. Subsequent analysis revealed good agreement between the theoretical predictions and experimental results for IR, Raman, and UV-VIS spectra. Among the functionals used, the BP86 functional demonstrated greater accuracy in predicting electronic transitions. It was observed that variations in the basis set size had minimal impact on the predicted UV-VIS spectra. However, inclusion of the polarizable continuum model and exclusion of the Tamm-Dancoff approximation were necessary to achieve optimal agreement with experimental measurements. These findings are valuable for future simulations of pharmaceutical compounds and for qualitative and quantitative assessment of GS-441524 in (unregulated) antiviral drugs for example, with portable IR/Raman spectrophotometers. Future theoretical work may focus on a detailed analysis of the available NMR spectra [37], [38], [39], [40], [29], providing deeper insights into the structural and dynamic properties of the system. We hope that GS-441524 will soon be approved in more countries, allowing for its legal use to save countless cats' lives.

Acknowledgements

The computational part of this work was funded through the Royal Society of Chemistry (RSC, UK) COVID-19 Head of Department Grant (H20-134). We wish to thank Dr E. I. Kamitsos for his kind interest and support for our work. Dr L. Zou (Gaussian Inc.) is acknowledged for many useful discussions. SM gratefully acknowledges Prof. A. Koutselos (National and Kapodistrian University of Athens, Greece), for his generous hospitality during his sabbatical leave.

References

[1] V. E. Kataev and B. F. Garifullin, "Antiviral nucleoside analogs", *Chem Heterocycl Comp*, vol. 57, no. 4, pp. 326–341, May 2021, doi: 10.1007/s10593-021-02912-8

[2] "Nucleoside Analogues", in *LiverTox: Clinical and Research Information on Drug-Induced Liver Injury*, Bethesda (MD): National Institute of Diabetes and Digestive and Kidney Diseases, 2012. Accessed: Jan. 25, 2024. [Online]. Available: http://www.ncbi.nlm.nih.gov/books/NBK548938/

[3] B. G. Murphy, M. Perron, E. Murakami, K. Bauer, Y. Park, C. Eckstrand, et al., "The nucleoside analog GS-441524 strongly inhibits feline infectious peritonitis (FIP) virus in tissue culture and experimental cat infection studies", *Vet. Microbiol.*, vol. 219, pp. 226–233, Apr. 2018, doi: 10.1016/j.vetmic.2018.04.026

[4] Z. Huang, L. Gong, Z. Zheng, Q. Gao, X. Chen, Y. Chen, et al., "GS-441524 inhibits African swine fever virus infection in vitro", *Antivir. Res.*, vol. 191, Art. no. 105081, Jul. 2021, doi: 10.1016/j.antiviral.2021.105081

[5] Y. Li, L. Cao, G. Li, F. Cong, Y. Li, J. Sun, et al., "Remdesivir Metabolite GS-441524 Effectively Inhibits SARS-CoV-2 Infection in Mouse Models", *J. Med. Chem.*, vol. 65, no. 4, pp. 2785–2793, Feb. 2022, doi: 10.1021/acs.jmedchem.0c01929

[6] H. Vennema, R. J. de Groot, D. A. Harbour, M. Dalderup, T. Gruffydd-Jones, M. C. Horzinek, et al., "Early death after feline infectious peritonitis virus challenge due to recombinant vaccinia virus immunization", *J. Virol.*, vol. 64, no. 3, pp. 1407–1409, Mar. 1990, doi: 10.1128/jvi.64.3.1407-1409.1990

[7] A. M. Izes, J. Yu, J. M. Norris, and M. Govendir, "Current status on treatment options for feline infectious peritonitis and SARS-CoV-2 positive cats", *Vet. Q.*, vol. 40, no. 1, pp. 322–330, Jan. 2020, doi: 10.1080/01652176.2020.1845917

[8] M. Dunowska and S. Ghosh, "*In Vitro* effects of doxycycline on replication of feline coronavirus", *Pathogens*, vol. 10, no. 3, Art. no. 312, Mar. 2021, doi: 10.3390/pathogens10030312

[9] N. C. Pedersen, "An update on feline infectious peritonitis: Diagnostics and therapeutics", *Vet. J.*, vol. 201, no. 2, pp. 133–141, Aug. 2014, doi: 10.1016/j.tvjl.2014.04.016

[10] D. Addie, L. Houe, K. Maitland, G. Passantino, N. Decaro, "Effect of cat litters on feline coronavirus infection of cell culture and cats", *J. Feline Med. Surg.*, vol. 22, no. 4, pp. 350–357, May 2020, doi: 10.1177/1098612X19848167

[11] S. Jones, W. Novicoff, J. Nadeau, S. Evans, "Unlicensed GS-441524-like antiviral therapy can be effective for at-home treatment of feline infectious peritonitis", *Animals* (Basel), vol. 11, no. 8, Art. no. 2257, Jul. 2021, doi: 10.3390/ani11082257

[12] S. Sorrell, S. J. Pugalendhi, D. Gunn-Moore, "Current treatment options for feline infectious peritonitis in the UK", *Compan. Animal*, vol. 27, no. 6, pp. 79–90, Jun. 2022, doi: 10.12968/coan.2022.0016

[13] D. Krentz, M. Bergmann, S. Felten, K. Hartmann, "Optionen zur therapie der felinen infektiösen peritonitis – früher und heute", *Tierarztl Prax Ausg K Kleintiere Heimtiere*, vol. 51, no. 05, pp. 351-360, Nov. 2023, doi: 10.1055/a-2147-3999

[14]"Delivering Transformative Therapies and Advancing Health Equity," Gilead. Accessed: Feb. 06, 2024. [Online]. Available: https://www.gilead.com

[15]F. Muller, "GS-441524 for COVID19 not pursued by GILEAD," Patent Opposition Database. Accessed: Feb. 06, 2024. [Online]. Available: https://www.patentoppositions.org/en/call_for_helps/5ed283dfd2708f000553d358

[16] M. Katayama and Y. Uemura, "Therapeutic effects of Mutian® Xraphconn on 141 client-owned cats with feline infectious peritonitis predicted by total bilirubin levels", *Vet. Sci.*, vol. 8, no. 12, Art. no. 328, Dec. 2021, doi: 10.3390/vetsci8120328

[17] A. R. Van Rompay, M. Johansson, A. Karlsson, "Phosphorylation of nucleosides and nucleoside analogs by mammalian nucleoside monophosphate kinases", *Pharmacol. Ther.*, vol. 87, no. 2–3, pp. 189–198, Mar. 2000, doi: 10.1016/S0163-7258(00)00048-6

[18] D. Wei, T. Hu, Y. Zhang, W. Zhang, H. Xue, J. Shen, et al., "Potency and pharmacokinetics of GS-441524 derivatives against SARS-CoV-2", *Bioorg. Med. Chem.*, vol. 46, Art. no. 116364, Sep. 2021, doi: 10.1016/j.bmc.2021.116364

[19] M. J. Frisch, G. W. Trucks, H. B. Schlegel, G. E. Scuseria, M. A. Robb, J. R. Cheeseman, et al., (2019). *Gaussian 16*, revision C.01, Wallingford, Connecticut: Gaussian, Inc. Available: https://gaussian.com/gaussian16

[20] R. Dennington, T. A. Keith, J. M. Millam (2016), *GaussView 6*, Wallingford, Connecticut: Gaussian, Inc. Available: https://gaussian.com/gaussview6

[21] C. Lee, W. Yang, R. G. Parr, "Development of the Colle-Salvetti correlation-energy formula into a functional of the electron density", *Phys. Rev. B*, vol. 37, no. 2, pp. 785–789, Jan. 1988, doi: 10.1103/PhysRevB.37.785

[22] M. Orio, D. A. Pantazis, F. Neese, "Density functional theory", *Photosynth. Res.*, vol. 102, no. 2–3, pp. 443–453, Nov. 2009, doi: 10.1007/s11120-009-9404-8

[23] T. Yanai, D. P. Tew, N. C. Handy, "A new hybrid exchange–correlation functional using the Coulomb-attenuating method (CAM-B3LYP)", *Chem. Phys. Lett.*, vol. 393, no. 1–3, pp. 51–57, Jul. 2004, doi: 10.1016/j.cplett.2004.06.011

[24] J. Tomasi, B. Mennucci, R. Cammi, "Quantum mechanical continuum solvation models", *Chem. Rev.*, vol. 105, no. 8, pp. 2999–3094, Aug. 2005, doi: 10.1021/cr9904009

[25] A. Allouche, "Gabedit—A graphical user interface for computational chemistry softwares", *J. Comput. Chem.*, vol. 32, no. 1, pp. 174–182, Jan. 2011, doi: 10.1002/jcc.21600

[26] G. Socrates, *Infrared and Raman Characteristic Group Frequencies: Tables and Charts*. 3rd ed. Chichester, West Sussex: UK: Wiley, 2001.

[27] A. Alrooqi, Z. M. Al-Amshany, L. M. Al-Harbi, T. A. Altalhi, M. S. Refat, A. M. Hassanien, et al., "Spectroscopic and physicochemical studies on 1,2,4-triazine derivative", *Coatings*, vol. 12, no. 5, Art. no. 714, May 2022, doi: 10.3390/coatings12050714

[28] D. Thastum Bach, F. Hegelund, J. A. Beukes, F. M. Nicolaisen, M. H. Palmer, "The high-resolution infrared spectrum of 1,2,4-triazine vapor between 550 and 1700 cm^{-1}", *J. Mol. Spectrosc.*, vol. 198, no. 1, pp. 77–93, Nov. 1999, doi: 10.1006/jmsp.1999.7935

[29] A. J. Mulligan and M. E. Browning, "Quality assessment and characterization of unregulated antiviral drugs for feline infectious peritonitis: implications for treatment, safety, and efficacy", *Am. J. Vet. Res.*, vol. 85 (3) pp. 1–9, Jan. 2024, doi: 10.2460/ajvr.23.10.0221

[30] S. Hirata and M. Head-Gordon, "Time-dependent density functional theory within the Tamm–Dancoff approximation", *Chem. Phys. Lett.*, vol. 314, no. 3–4, pp. 291–299, Dec. 1999, doi: 10.1016/S0009-2614(99)01149-5

[31] R. G. Parr and Y. Weitao, *Density-Functional Theory of Atoms and Molecules*, Oxford: Oxford University Press 1994

[32] L. E. Chirlian and M. M. Francl, "Atomic charges derived from electrostatic potentials: A detailed study", *J. Comput. Chem.*, vol. 8, no. 6, pp. 894–905, Sep.1987, doi: 10.1002/jcc.540080616

[33] C. M. Breneman and K. B. Wiberg, "Determining atom-centered monopoles from molecular electrostatic potentials. The need for high sampling density in formamide conformational analysis", *J. Comput. Chem.*, vol. 11, no. 3, pp. 361–373, Apr. 1990, doi: 10.1002/jcc.540110311

[34] H. Hu, Z. Lu, W. Yang, "Fitting Molecular Electrostatic Potentials from Quantum Mechanical Calculations", *J. Chem. Theory Comput.*, vol. 3, no. 3, pp. 1004–1013, May 2007, doi: 10.1021/ct600295n

[35] U. Chandra Singh and P. A. Kollman, "An approach to computing electrostatic charges for molecules", *J. Comput. Chem.*, vol. 5, no. 2, pp. 129–145, Apr. 1984, doi: 10.1002/jcc.540050204

[36] B. H. Besler, K. M. Merz, P. A. Kollman, "Atomic charges derived from semiempirical methods", *J. Comput. Chem.*, vol. 11, no. 4, pp. 431–439, May 1990, doi: 10.1002/jcc.540110404

[37] T. K. Warren, R. Jordan, M. K. Lo, A. S. Ray, R. L. Mackman, V. Soloveva, et al., "Therapeutic efficacy of the small molecule GS-5734 against Ebola virus in rhesus monkeys", *Nature*, vol. 531, no. 7594, pp. 381-385, Mar. 2016, doi:10.1038/nature17180

[38] D. Krentz, K. Zenger, M. Alberer, S. Felten, M. Bergmann, R. Dorsch, et al., "Curing cats with feline infectious peritonitis with an oral multi-component drug containing GS-441524", *Viruses*, vol. 13, no. 11, 2228, Nov. 2021, doi:10.3390/v13112228

[39] A. C. Tsika, A. Gallo, N. K. Fourkiotis, A. I. Argyriou, S. Sreeramulu, F. Löhr, et al., "Binding adaptation of GS-441524 diversifies macro domains and down-regulates SARS-CoV-2 de-

MARylation capacity", *J. Mol. Biol.*, vol. 434, no. 16, Art. no. 167720, Jul. 2022, doi: 10.1016/j.jmb.2022.167720

[40] A. Furbish, M. Allinder, G. Austin, B. Tynan, E. Byrd, I. Pina Gomez, et al., "First analytical confirmation of drug-induced crystal nephropathy in felines caused by GS-441524, the active metabolite of Remdesivir", *J. Pharm. Biomed. Anal.* vol. 247, Art. no. 116248, Sep. 2024, doi:10.1016/j.jpba.2024.116248

Appendix A. Supplementary material

Supplementary data associated with the article can be found in the online version at doi: 10.25103/jestr.175.01S1

Table S1. B3LYP/6-311++G(d,p) optimized geometry of GS-441524

Table S2. BP86/6-311++G(d,p) optimized geometry of GS-441524.

Table S3. CAM-B3LYP/6-311++G(d,p) optimized geometry of GS-441524.

Table S4. Vibrational assignment for the experimentally observed FT-IR and Raman wavenumbers (cm^{-1}) and comparison with BP86/6-311++G(d,p) calculations.

Table S5. Atomic charge analysis of GS-441524 in water at B3LYP/6-311++G(d,p) level of theory.

Fig. S1. Surface plot of the electrostatic potential of GS-441524 in water solvent at the B3LYP/6-311++G(d,p) level of theory.

Supplementary files:

Data points from Raman experimental spectrum.txt (doi: 10.25103/jestr.175.01S2)

Data points from IR experimental spectrum.txt (doi: 10.25103/jestr.175.01S3)